

Article

Crystal Structure, Hydration, and Two-Fold/Single-Fold Diffusion Kinetics in Proton-Conducting $\text{Ba}_{0.9}\text{La}_{0.1}\text{Zr}_{0.25}\text{Sn}_{0.25}\text{In}_{0.5}\text{O}_{3-a}$ Oxide

Wojciech Skubida ¹, Anna Niemczyk ¹, Kun Zheng ¹ , Xin Liu ² and Konrad Świczek ^{1,3,*} 

¹ Faculty of Energy and Fuels, Department of Hydrogen Energy, AGH University of Science and Technology, al. A. Mickiewicza 30, 30-059 Krakow, Poland; wskubida@agh.edu.pl (W.S.); niemczyk@agh.edu.pl (A.N.); zheng@agh.edu.pl (K.Z.)

² Contemporary Amperex Technology Co., Limited, Fujian 352100, China; rzxhygr@163.com

³ AGH Centre of Energy, AGH University of Science and Technology, ul. Czarnowiejska 36, 30-054 Krakow, Poland

* Correspondence: xi@agh.edu.pl

Received: 15 February 2018; Accepted: 13 March 2018; Published: 16 March 2018

Abstract: In this work, hydration kinetics related to the incorporation of water into proton-conducting $\text{Ba}_{0.9}\text{La}_{0.1}\text{Zr}_{0.25}\text{Sn}_{0.25}\text{In}_{0.5}\text{O}_{3-a}$ perovskite-type oxide are presented, with a recorded transition on temperature from a single-fold to a two-fold behavior. This can be correlated with an appearance of the electronic hole component of the conductivity at high temperatures. The collected electrical conductivity relaxation data allowed to calculate chemical diffusion coefficient D and surface exchange reaction coefficient k , as well as respective activation energies of their changes on temperature. Presented results are supplemented with a systematic characterization of the structural properties of materials synthesized at different temperatures, amount of incorporated water after hydration in different conditions, influence of water content on the crystal structure, as well as electrical conductivity in dry, H_2O - and D_2O -containing air, which enabled to evaluate proton (deuterium) conductivity.

Keywords: perovskite oxides; substituted barium indate; hydration; proton conductivity; relaxation experiments; coupled/decoupled ionic transport

1. Introduction

High-temperature proton conductors, used e.g., as electrolytes in Protonic Ceramic Fuel Cell (PCFC) technology, are characterized by a high ionic conductivity at the intermediate temperatures (ca. 500–700 °C), which may surpass the one of commonly used oxide ion conductors [1,2]. The first reports on proton-conducting ceramics were presented by Iwahara and co-workers in the 1980s [3,4]. Since that time, many acceptor-doped $\text{AB}_{1-x}\text{M}_x\text{O}_{3-\delta}$ (A: Ba, Sr, Ca; B: Zr, Ce, In, Sn; M: different +3/+2 elements) perovskite-type oxides were discovered and characterized as efficient proton conductors [5–10].

One of the highest values of H^+ conductivity in wet atmospheres, on the order of $10^{-2} \text{ S cm}^{-1}$ at ca. 600 °C, show materials based on BaCeO_3 . At higher temperatures, their total ionic conductivity increases even more, but oxygen ion component becomes predominant, which results in a significant decrease of the proton transfer number t_{H} [11,12]. Unfortunately, cerium-based perovskites react with acidic oxides (e.g., CO_2 or SO_3) and steam, forming carbonates and hydroxides, which limits usage of these materials in fuel cells or high temperature steam electrolyzers [13,14]. Zr-based oxides exhibit improved stability, but their proton conductivity is lower and much higher temperatures are required for a successful sintering of dense pellets/membranes [15,16]. Recently, other materials having different crystal structures are also considered as high-temperature proton conductors [17–24].

Proton, due to a lack of electrons on its electron shell, strongly polarizes surrounding ions in a host lattice, leading to the formation of a relatively high-energy bonds nearby. Consequently, protons in oxides are located in the electron cloud of the oxygen anions, forming OH_O^\bullet defects [17]. Depending on the atmosphere, protons can be absorbed into the oxide structure according to the following reactions [25]:

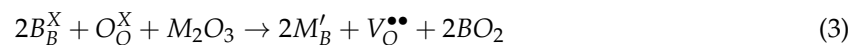
- in dry hydrogen atmosphere,



- in humidified atmosphere,



For the second reaction, commonly observed for perovskite-type oxides, the presence of the oxygen vacancies in the crystal structure is required. In the $A^{2+}B^{4+}O_3$ perovskite oxides, partial substitution of the B-site cation by e.g., trivalent one (M^{3+}) is used to form the oxygen vacancies [13].



The amount of the oxygen vacancies is therefore half of the introduced M^{3+} . Simulations and isotopic studies have suggested that the Grotthuss mechanism can be generally considered as the proton transport mechanism, occurring at elevated temperatures in perovskite oxides [26]. It is known that the activation energy of proton hopping from one oxygen anion to the neighboring one depends on the oxygen-oxygen distance, but regardless of the crystal structure of the oxides, the value is about 2/3 of the activation energy of the oxygen transport through the vacancy mechanism. This can be explained by the fact that the migration of protons is completely dependent on the oscillation of the oxygen network. For both types of conductivity, the charge carriers need to overcome the same energy barrier, but while the oxygen anion must go through the so-called saddle point between the energy minima, the proton can jump (or tunnel) when the ion on which it is located will overcome 2/3 of the height of the energy barrier [27].

It is also known that there is a correlation between a difference of electronegativity of the A- and the B-site cations and the enthalpy of the hydration reaction. If the electronegativity difference is higher, it limits the amount of incorporated protons, lowering the proton conductivity [28].

Coupled and Decoupled Diffusion of Ionic Charge Carriers

Considering Equation (2), the respective equation for the reaction's constant can be written as

$$K_W = \frac{[OH_O^\bullet]^2}{p_{H_2O} [V_O^{\bullet\bullet}] [O_O^X]} \quad (4)$$

Also, Equations (3) and (4) can be re-written in the following form [29]:



$$K'_W = \frac{[H_i^\bullet]^2 [O_O^X]}{p_{H_2O} [V_O^{\bullet\bullet}]} \quad (6)$$

As noticed in work [29], this should correspond to the situation that during incorporation (or release) of water into (from) the oxide, the diffusion of the oxygen anions and protons is ambipolar. In other words, respective fluxes are correlated to each other. Consequently, in e.g., the electrical relaxation experiments conducted during change of the water vapor partial pressure in the sample's surrounding atmosphere, the respective relaxation curves should be of a single fold nature. This is in contrast to numerous literature reports showing a two-fold character of the relaxation curves recorded in specific conditions [30–36].

In a new approach presented in work [29], the two-fold relaxation kinetics are explained by a decoupled transport of hydrogen and oxygen ions, which initially occurs on the surface and is followed by diffusion in the bulk.



This corresponds to the situation of decoupled chemical diffusion of hydrogen and oxygen. Both processes can be described, respectively, as ambipolar diffusion of protons and electronic holes, as well as ambipolar diffusion of oxygen anions and electronic holes. Furthermore, as shown in work [30], the observed change in the total conductivity ($\Delta\sigma$) as a function of time (i.e., in relaxation experiments) is a sum of the H-related and O-related conductivities, which proceed in opposite directions: $\Delta\sigma(H)$ is decreasing with time, while $\Delta\sigma(O)$ is increasing.

Crucial for the relaxation behavior is the presence of electronic holes, generated according to the Equation (9) and consumed in Equation (8). If their concentration is negligible, the corresponding transference number of the hole conductivity approaches zero. In this case, the decoupled transport (two-fold relaxation kinetics) reduces to the single-fold diffusion of water (single-fold relaxation) [29].

In this paper, comprehensive results of structural, thermogravimetric, and transport properties of proton-conducting $Ba_{0.9}La_{0.1}Zr_{0.25}Sn_{0.25}In_{0.5}O_{3-a}$ oxide are presented. Notwithstanding that the chosen chemical composition is not characterized by a very high proton conductivity, it enabled us to observe the temperature-dependent transition from the single-fold to the two-fold relaxation kinetics associated to the appearance of the electronic hole-related conductivity. Apart from the characterization of the basic physicochemical properties, the conducted studies with humidified atmosphere allowed us to determine the values of the activation energy of the surface exchange coefficient k and the bulk diffusion coefficient D for the coupled and decoupled ionic transport.

2. Materials and Methods

Analyzed $Ba_{0.9}La_{0.1}Zr_{0.25}Sn_{0.25}In_{0.5}O_{3-a}$ was synthesized by a standard high-temperature solid state route. Stoichiometric amounts of the respective oxides (La_2O_3 , ZrO_2 , SnO_2 , In_2O_3) and barium carbonate ($BaCO_3$), all with $\geq 99.9\%$ purity, were homogenized in a high-efficiency mill. The used La_2O_3 was earlier preheated up to $800\text{ }^\circ\text{C}$ in order to remove water and ensure proper stoichiometry. The obtained mixture was pressed into pellets and then annealed in a temperature range of $1200\text{--}1450\text{ }^\circ\text{C}$. For preparation of dense pellets (ca. 98%), the initial calcination performed at $950\text{ }^\circ\text{C}$ in synthetic air (decomposition of $BaCO_3$) was required, and also, the sintering temperature was increased up to $1600\text{ }^\circ\text{C}$. In order to minimize evaporation of barium or other cations, the pressed pellets were covered with a layer of a powder having the same composition and were placed in lid-covered crucibles. Chemical composition of the materials was established by inductively coupled plasma-optical emission spectroscopy (ICP-OES, Optima 2100, Perkin Elmer, Wellesley, MA, USA).

Structural data were obtained by X-ray diffraction (XRD) measurements conducted in $10^\circ\text{--}110^\circ$ range using CuK_α radiation on Panalytical Empyrean diffractometer (Empyrean, Panalytical, Almelo, Netherlands) equipped with PIXcel3D detector. An Anton Paar HTK 1200N (Panalytical, Almelo, The Netherlands) oven chamber was used for high-temperatures XRD studies, which were carried out in $25\text{--}900\text{ }^\circ\text{C}$ temperature range in a synthetic air flow (H_2O content < 3 ppm). Structural parameters were refined using GSAS/EXPGUI set of software, based on Rietveld method (a least squares approach, which enable to refine a theoretical XRD profile until it matches the measured data) [37,38]. In the fittings done using cubic $Pm\text{-}3m$ space group, unit cell parameter a , profile parameters, zero shift, and thermal U_{iso} factors were refined. It should be emphasized that (Ba,La)-O distance can be derived as equal to $a\sqrt{2}/2$, while (Zr,Sn,In)-O bond length equals $a/2$ in the cubic perovskite structure. Stored

and dried at 400 °C for 24 h (in synthetic air), the materials were studied during XRD measurements. Also, Scherrer equation was utilized to obtain crystallite size.

Microstructure of the as-synthesized materials was analyzed by scanning electron microscopy (SEM) technique. SEM images were taken on FEI Nova NanoSEM 200 apparatus (FEI EUROPE COMPANY, Eindhoven, The Netherlands).

In order to evaluate the amount of the incorporated water, thermogravimetric (TG) measurements were carried out on TA Q5000 IR thermobalance (TA Instruments, New Castle, DE, USA). Tests were performed up to 900 °C (heating/cooling rate 5 °C min⁻¹) in synthetic air on previously hydrated and dried samples. The hydration process was conducted by annealing of Ba_{0.9}La_{0.1}Zr_{0.25}Sn_{0.25}In_{0.5}O_{3-a} powder at 250 °C and 400 °C in humidified air (ca. 3% vol. H₂O), while drying was done by similar annealing at 400 °C and 800 °C in synthetic air. TG measurements were accompanied by mass spectroscopy analysis of the out-going gas in order to establish H₂O and CO₂ presence in the studied samples. For the studies, Pfeiffer Vacuum ThermoStar mass spectrometer (GSD 301 T1 (2008/08), Pfeiffer Vacuum, Aßlar, Germany) was used. The initial and relatively high water signal recorded in the studies likely comes from the apparatus-related affect (presence of residual moisture). This line should be treated as a background one.

Electrical properties of a dense Ba_{0.9}La_{0.1}Zr_{0.75}Sn_{0.75}In_{0.5}O_{3-a} sinter were measured by the AC electrochemical impedance spectroscopy (EIS) technique using Solartron 1260 frequency response analyzer (1260, Solartron, Bognor Regis, Great Britain). Samples were mounted on Probostat holder, with Pt electrodes attached. The applied disturbance amplitude was 25 mV and the frequency range was 0.1–10⁶ Hz. Tests were performed in 350–800 °C temperature range in dry synthetic air, and also in humidified synthetic air with H₂O and D₂O (ca. 3% vol.) in order to establish proton (deuterium) conductivity component of the total conductivity. Additional measurements were conducted in dry and H₂O-containing argon to evaluate *p*O₂ influence on conductivity. Gathered data were analyzed using Scribner Associates Inc. ZView 2.9 software (Scribner Associates Inc., Southern Pines, NC, USA) by selection of a proper equivalent electrical circuit [39]. An approximate value of proton conductivity (σ_H) was obtained as a difference between the recorded conductivity in wet and dry atmospheres: $\sigma_H = \sigma_{\text{wet}} - \sigma_{\text{dry}}$. Consequently, the transference number $t_H = \sigma_H / \sigma_{\text{wet}}$. Similar calculations were carried out in the case of measurements in D₂O-containing atmosphere in order to determine σ_D and t_D [40].

Electrical conductivity relaxation (ECR) measurements were performed during an abrupt gas change from dry to humidified synthetic air at the constant temperature in a range of 350–800 °C. The recorded ECR profiles were normalized and refined using custom-made Matlab code. Considering geometry of the pellets, the one-dimensional diffusion model was found to be the correct approximation [41]. Interestingly, a coupled and decoupled transport phenomena related to the ionic conductivity were observed. While these effects were previously reported in several studies [34,36], for the presented results, a clear transition occurs as a function of temperature.

3. Results and Discussion

3.1. Crystal Structure at Room and Elevated Temperatures

As shown in Figure 1a, Ba_{0.9}La_{0.1}Zr_{0.25}Sn_{0.25}In_{0.5}O_{3-a} oxide can be obtained as a single phase, with no major impurities present in a wide range of temperatures (1200–1600 °C). Figure 1b shows an exemplary diffractogram recorded at room temperature (RT) of a sample after heat treatment at 1400 °C, together with the performed structural refinement. It can be seen that all reflections correspond well with the cubic *Pm-3m* space group. This structure was present in all samples sintered at different temperatures. It is also visible (Figure 1a) that, with the increasing sintering temperature, the recorded peaks shift toward higher angles, suggesting a decrease of the unit cell parameter. This was confirmed by Rietveld refinements, and the calculated dependence is shown in Figure 2. In order to establish chemical composition of the samples, ICP studies were conducted, with results being in agreement with the assumed content of the elements (e.g., material annealed at

1400 °C has $\text{Ba}_{0.93}\text{La}_{0.10}\text{Zr}_{0.22}\text{Sn}_{0.29}\text{In}_{0.49}\text{O}_{2.84}$ composition). In addition, these measurements indicated somewhat increased evaporation of barium, as well as tin and indium for materials annealed at higher temperatures, but the changes were found to be rather too small to fully explain the decrease of the a parameter with the sintering temperature (both Ba^{2+} and In^{3+} are large cations). Alternatively, it seems that the observed variation of the unit cell parameter mainly originates from a high affinity of the samples for water incorporation. For comparison, XRD measurements were also conducted immediately after drying of the samples in synthetic air at 400 °C for 24 h. The refined unit cell parameters are significantly lower (except for the material sintered at 1600 °C), suggesting that the compounds stored under ambient conditions reacted with moisture from air.

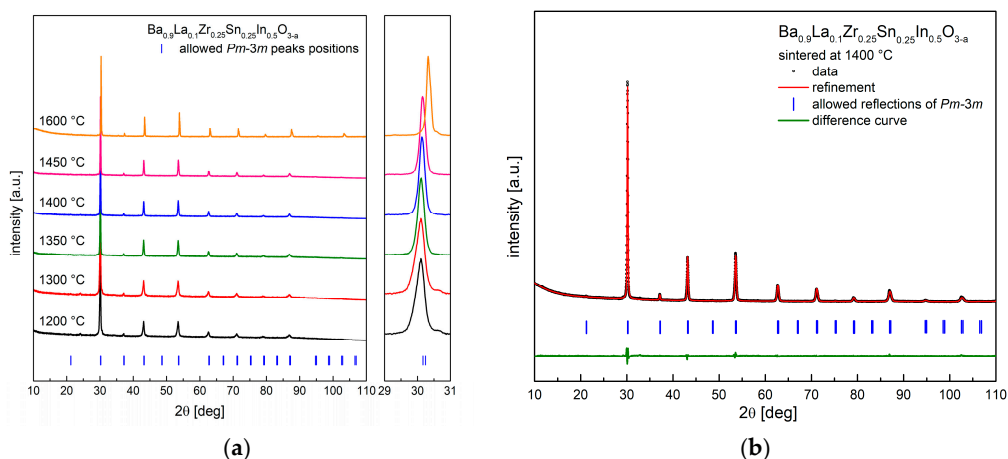


Figure 1. (a) X-ray diffraction (XRD) data recorded at room temperature (RT) for samples sintered at different temperatures; (b) XRD diffractogram with Rietveld refinement for $\text{Ba}_{0.9}\text{La}_{0.1}\text{Zr}_{0.25}\text{Sn}_{0.25}\text{In}_{0.5}\text{O}_{3-a}$ sintered at 1400 °C.

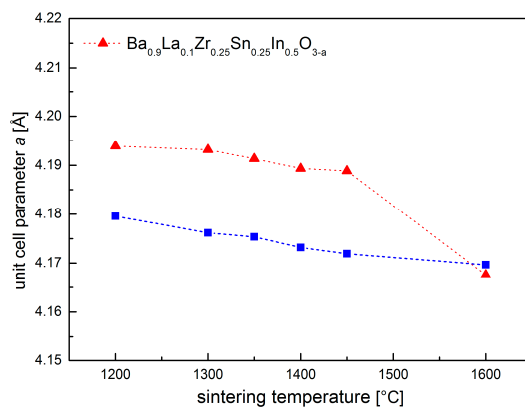


Figure 2. Unit cell parameter a dependence on the sintering temperature for $\text{Ba}_{0.9}\text{La}_{0.1}\text{Zr}_{0.25}\text{Sn}_{0.25}\text{In}_{0.5}\text{O}_{3-a}$.

As the temperature of the synthesis increases, the average crystallite size was found to grow in the expected manner (Figure 3). Nevertheless, the pellets obtained at 1450 °C and below are not well-sintered, with a relative density not exceeding 70%. On the contrary, material prepared at 1600 °C was very dense (ca. 98%). Consequently, a large surface area of contact between the material and atmospheric air of the porous specimens (Figure 4) intensifies reactivity with the water vapor, while for the dense material, only the pellet's surface has direct contact with the atmosphere, suppressing the reaction. This is of a crucial consequence because $\text{Ba}_{0.9}\text{La}_{0.1}\text{Zr}_{0.25}\text{Sn}_{0.25}\text{In}_{0.5}\text{O}_{3-a}$ in a powder form is reactive toward H_2O at very low temperatures, even at RT.

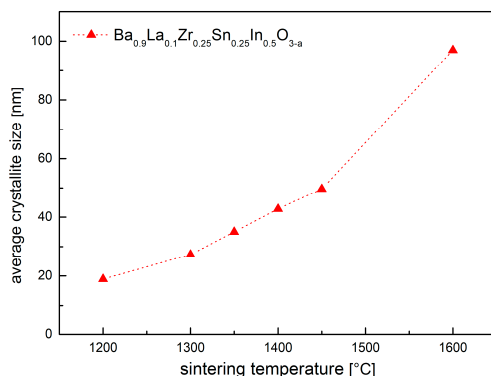


Figure 3. Calculated average crystallite size of $Ba_{0.9}La_{0.1}Zr_{0.25}Sn_{0.25}In_{0.5}O_{3-a}$ as a function of the sintering temperature.

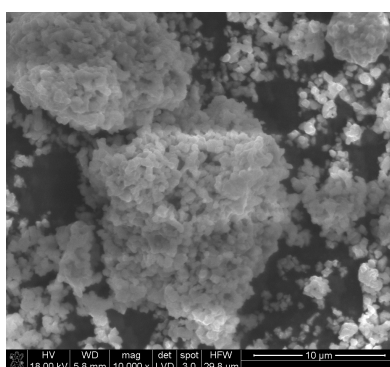


Figure 4. Scanning electron microscopy (SEM) micrograph of $Ba_{0.9}La_{0.1}Zr_{0.25}Sn_{0.25}In_{0.5}O_{3-a}$ material (crushed and grinded pellet) sintered at 1400 °C.

As shown in Figure 5, material sintered at 1400 °C and dried at 400 °C in synthetic air, which was protected from the ambient atmosphere and studied in a short time after the synthesis, exhibits much lower unit cell parameter (4.1742 Å), comparing to the one stored under ambient conditions (4.1894 Å). The effect of the unit cell parameter (and volume) increase on hydration of the material was previously documented in works [42–44].

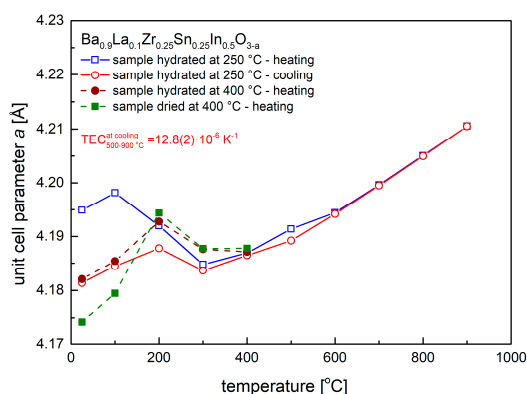


Figure 5. Unit cell parameter dependence on temperature, as calculated from high-temperature XRD data, recorded in synthetic air for samples, which were previously hydrated at 250 °C and 400 °C, as well as dried at 400 °C.

With an initial increase of temperature above RT, the material dried at 400 °C was found to increase its unit cell parameter (and volume) up to 200 °C, above which temperature the recorded unit cell parameter decreased and then increased again above 400 °C (Figure 5). Essentially the same behavior was observed for samples previously hydrated in humidified synthetic air (ca. 3 vol. % H₂O) at 250 °C and 400 °C. The quantitative difference between the materials results from the value of the initial unit cell parameter, which was found to be the highest for the oxide hydrated at 250 °C. As documented below in TG studies, this corresponds to the highest amount of the incorporated water into the crystal structure. Above ca. 400 °C all studied samples were found to behave practically the same. During cooling from 900 °C to 500 °C the relative changes of the unit cell parameter scaled linearly with temperature, which allowed to evaluate thermal expansion coefficient (TEC). The TEC value was found to be moderate, $12.8(2) \times 10^{-6} \text{ K}^{-1}$, a typical one for this class of materials. Interestingly, on cooling below 300 °C, the unit cell parameter of Ba_{0.9}La_{0.1}Zr_{0.25}Sn_{0.25}In_{0.5}O_{3-a} increased and then decreased again. This effect can be explained as due to incorporation of residual water vapor present in synthetic air, and while H₂O content is below 3 ppm, a constant gas flow on the order of 100 cm³ min⁻¹ supplied into the oven-chamber was enough for the sample to absorb relatively large quantity of water [45–47].

Selected data concerning structural refinements performed at RT and at elevated temperatures are gathered in Table 1 below.

Table 1. Refined structural data for Ba_{0.9}La_{0.1}Zr_{0.25}Sn_{0.25}In_{0.5}O_{3-a} material obtained in different conditions.

Conditions	Unit Cell Parameter <i>a</i> [Å]	Unit Cell Volume <i>V</i> [Å ³]	(Ba,La)-O Distance [Å]	(Zr,Sn,In)-O Distance [Å]	χ ² /R _{wp} [%]	U _{iso} ·100 [Å ²] CationsO
stored sample	4.1893(1)	73.53(1)	2.9623(1)	2.0947(1)	4.125/3.53	2.39(2)/4.6(1)
material hydrated at 250 °C (data at RT)	4.1949(1)	73.82(1)	2.9662(1)	2.0974(1)	1.548/2.79	2.08(2)/3.1(1)
data recorded at 600 °C in synthetic air	4.1944(1)	73.79(1)	2.9659(1)	2.0972(1)	2.291/3.45	2.09(2)/4.3(2)
data recorded at 900 °C in synthetic air	4.2105(1)	74.64(1)	2.9773(1)	2.1053(1)	1.959/3.21	2.83(2)/5.7(2)

All of the presented above results can be explained as originating from a presence of protons in the studied material, which incorporation/release (in a form of water) on heating/cooling is visible in structural changes. What is more, strong effects recorded for the dried sample prove a very strong affinity of the material toward water uptake, even at very low water partial pressures.

3.2. Thermogravimetric Measurements and Presence of Protons

The results of thermogravimetric studies conducted in synthetic air for Ba_{0.9}La_{0.1}Zr_{0.25}Sn_{0.25}In_{0.5}O_{3-a} material hydrated at 250 °C are shown in Figure 6a. TG measurements were accompanied by mass spectroscopy studies, and the recorded (relative) ionic current data of H₂O- and CO₂-related signals are presented in Figure 6b,c. As can be seen, during first heating, a considerable weight loss occurs at above 200 °C, matching well the behavior seen in the high-temperature XRD studies for the hydrated material (Figure 5). The maximum signal of the H₂O occurs at lower temperature than the CO₂-related peak (Figure 6b,c), and consequently, it can be assumed that majority of the weight change up to ca. 300 °C is related to the water release. Using TG data the amount of the incorporated water during hydration at 250 °C can be estimated as ca. 0.13 mole of water per mole of material, corresponding to the Ba_{0.9}La_{0.1}Zr_{0.25}Sn_{0.25}In_{0.5}O_{2.93}H_{0.26} composition. For the material hydrated at 400 °C, the water content was found to be smaller, ca. 0.11. Interestingly, on the second TG cycle some remaining water signal was also recorded. For the CO₂ signal, while the first maximum can be linked to a desorption process from the powder's surface, the peak at ca. 600 °C can be related to a decomposition of residual carbonates. Apart

from the first heating, practically no CO₂-related signal was recorded in the following steps of the TG studies. Importantly, in additional studies of materials previously dried in synthetic air at 400 °C and 800 °C, qualitatively similar behavior was observed, i.e., presence of H₂O- and CO₂-related peaks was evident. This strongly indicates that samples are highly moisture- and CO₂-sensitive, even during contact with atmospheric air at ambient temperature for a relatively short time.

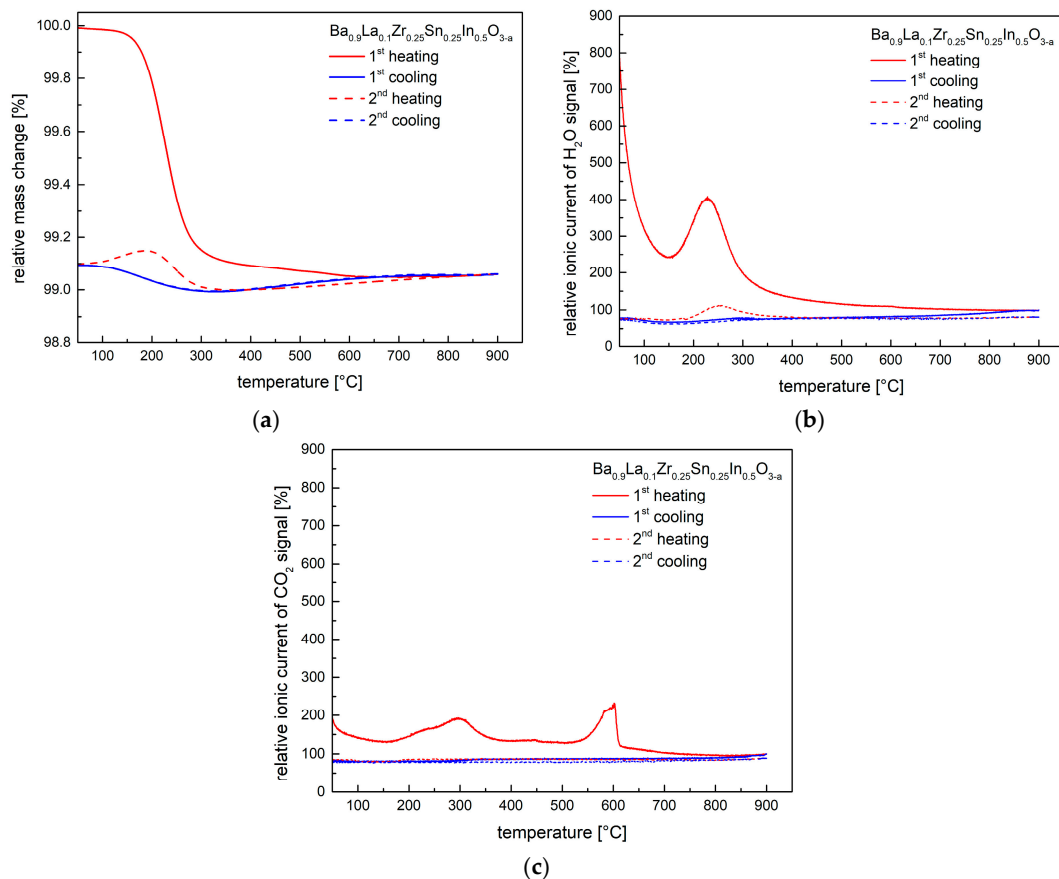


Figure 6. (a) Thermogravimetric characteristics for the hydrated at 250 °C $\text{Ba}_{0.9}\text{La}_{0.1}\text{Zr}_{0.25}\text{Sn}_{0.25}\text{In}_{0.5}\text{O}_{3-a}$ material, recorded in synthetic air during two cycles; (b) Relative ionic current of H₂O-related signal recorded by mass spectrometer, corresponding to the performed TG studies; (c) Relative ionic current of CO₂-related signal recorded by mass spectrometer, corresponding to the performed TG studies.

3.3. Transport Properties in Dry and Humidified Air

Figure 7a,b show exemplary impedance data with fitting, measured for the $\text{Ba}_{0.9}\text{La}_{0.1}\text{Zr}_{0.25}\text{Sn}_{0.25}\text{In}_{0.5}\text{O}_{3-a}$ material in different atmospheres at 450 °C and 750 °C. The spectra at the lower temperature contain three semi-circles. However, the refinements suggest the presence of the R_0 shift from the origin of coordinates (see inset with the equivalent circuit). Such results can be interpreted that the bulk and the grain boundary conductivities correspond to the shift and the high-frequency arc visible on the left, while charge transfer between the sample and the electrodes is visible in a form of the middle- and the low-frequency arc on the right [43,48]. There is a noticeable decrease of the high frequency arc and the shift upon change of the atmosphere from dry to H₂O (D₂O)-containing air, which is an evidence for the appearance of the proton (deuterium) conductivity. It is also expected that the relative increase of the conductivity related to D₂O is smaller [45]. EIS data recorded at higher temperatures, e.g., 750 °C (Figure 7b) are different, and strongly suggest presence of the electronic component of the conductivity, with R_0 shift from the origin of coordinates likely comprising also the ohmic resistance. This issue is discussed in more details below.

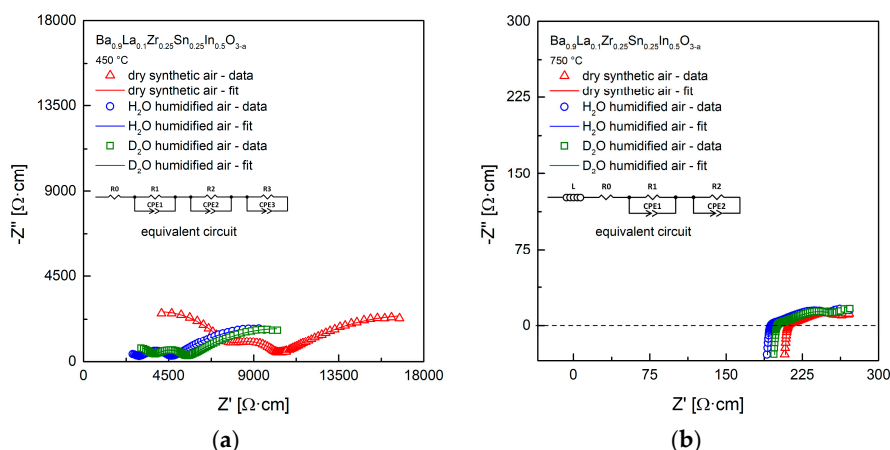


Figure 7. (a) Exemplary impedance data with fitting, measured in dry, H₂O-, and D₂O-containing synthetic air at 450 °C; (b) Exemplary impedance data with fitting, measured in dry, H₂O-, and D₂O-containing synthetic air at 750 °C.

Gathered impedance data allowed us to establish the temperature dependence of the total electrical conductivity, as presented in Arrhenius-type coordinates (Figure 8a). The results are expected, with the highest conductivity values and lowest activation energy appearing in H₂O-containing atmosphere. It can be noticed that the relative increase of the conductivity in wet atmospheres is not very high, and consequently the calculated proton (deuterium) conductivities and the respective transference numbers are not high (Table 2). The exemplary proton conductivities are ca. $1.1 \times 10^{-4} \text{ S cm}^{-1}$ at 350 °C and increase to $6.4 \times 10^{-4} \text{ S cm}^{-1}$ at 550 °C. A very similar dependence of total conductivity was observed in dry and wet Ar (Figure 8b), which suggest negligible influence of the oxygen partial pressure in this range, making the approximations about determination of proton and deuterium conductivities viable (electronic component is insignificant in such conditions).

At the highest temperatures of 700–800 °C, practically no change of the conductivity of the material during change of the atmosphere was recorded (Figure 8a,b). Considering the shape of the impedance data (Figure 7b), a large part of the resistance can be related to the electronic hole component. This was further supported by polarization-type (Hebb-Wagner) conductivity experiment, which allowed us to establish that, at 800 °C in dry air, the electronic component of the conductivity seems to be dominant. However, due to intrinsic limitations of the method, the exact evaluation of the electronic transference number was hindered.

Table 2. Calculated proton (σ_{H}) and deuterium (σ_{D}) conductivities together with respective transference numbers (t_{H} , t_{D}) for measurement conducted in synthetic air and argon.

Temperature [°C]	$\sigma_{\text{H}} = \sigma_{\text{wet}} - \sigma_{\text{dry}}$ [S cm ⁻¹]		$\sigma_{\text{D}} = \sigma_{\text{wet}} - \sigma_{\text{dry}}$ [S cm ⁻¹]		$t_{\text{H}} = \sigma_{\text{H}}/\sigma_{\text{wet}}$		$t_{\text{D}} = \sigma_{\text{D}}/\sigma_{\text{wet}}$
	Air	Ar	Air	Ar	Air	Ar	Air
650	5.0×10^{-4}	1.3×10^{-3}	3.3×10^{-4}		0.05	0.16	0.04
600	6.2×10^{-4}	9.5×10^{-4}	2.3×10^{-4}		0.08	0.16	0.03
550	6.4×10^{-4}	9.0×10^{-4}	1.5×10^{-4}		0.14	0.20	0.04
500	4.8×10^{-4}	7.1×10^{-4}	3.9×10^{-5}		0.17	0.25	0.02
450	4.1×10^{-4}	5.1×10^{-4}	1.9×10^{-4}		0.25	0.31	0.13
400	2.4×10^{-4}	2.9×10^{-4}	3.8×10^{-5}		0.30	0.33	0.06
350	1.1×10^{-4}	1.4×10^{-4}	2.6×10^{-5}		0.30	0.32	0.10

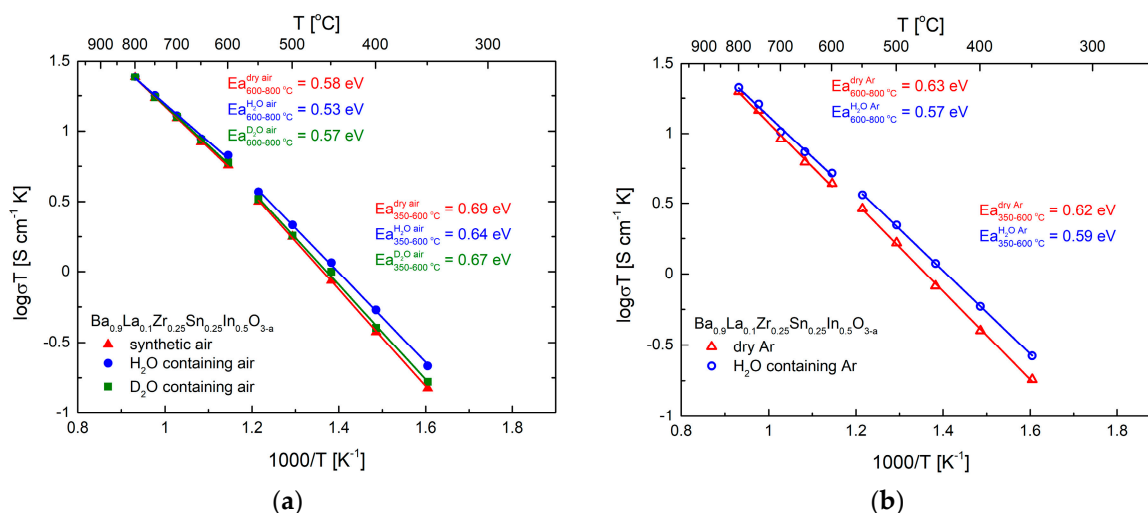


Figure 8. (a) Temperature dependence of the electrical conductivity of $\text{Ba}_{0.9}\text{La}_{0.1}\text{Zr}_{0.25}\text{Sn}_{0.25}\text{In}_{0.5}\text{O}_{3-a}$ in dry, H_2O -, and D_2O -containing air, with calculated values of the activation energy. Data shown in Arrhenius-type coordinates; (b) Temperature dependence of the electrical conductivity of $\text{Ba}_{0.9}\text{La}_{0.1}\text{Zr}_{0.25}\text{Sn}_{0.25}\text{In}_{0.5}\text{O}_{3-a}$ in dry and H_2O -containing Ar, with calculated values of the activation energy. Data shown in Arrhenius-type coordinates.

Overall, such electrical properties of $\text{Ba}_{0.9}\text{La}_{0.1}\text{Zr}_{0.25}\text{Sn}_{0.25}\text{In}_{0.5}\text{O}_{3-a}$ can be linked with a relatively low initial concentration of the oxygen vacancies, as well as with presence of Sn and in cations having relatively high electronegativity, and thus limiting proton (deuterium) conductivity at lower temperatures. Comparing to materials having higher initial oxygen vacancy concentration, the reported in Table 2 values of the proton conductivity are lower [43]. While from a point of view of application as PCFC solid electrolyte the material seems not suitable, for this compound, it was possible to record transition on temperature from a single-fold to a two-fold behavior on the electrical conductivity relaxation kinetics, indicating qualitative change of diffusion of the charge carriers, as presented in the next sub-chapter.

3.4. Conductivity Relaxations Studies upon Hydration

Figure 9a,b shows exemplary ECR data measured for the $\text{Ba}_{0.9}\text{La}_{0.1}\text{Zr}_{0.25}\text{Sn}_{0.25}\text{In}_{0.5}\text{O}_{3-a}$ material during an abrupt change of the surrounding atmospheres from dry to humidified air, as recorded at 450°C and 650°C . As can be seen, while the results from the lower temperature show single-fold character, data from the higher temperature are evidently pointing to a decoupled transport of hydrogen and oxygen. Using similar reasoning as presented in work [33], this corresponds to a qualitative change of the diffusion process, which from the coupled, ambipolar transfer of protons and oxygen (i.e., water) becomes decoupled, and both charge carriers move independently. Such change implies the presence of the electronic hole conductivity, as can be expected from the discussed characteristics of the EIS data recorded at higher ($\geq 600^{\circ}\text{C}$) temperatures. It should be clarified that, in the case of ECR profiles fitted at 600°C and above, only R_0 component was considered, which is in accordance with the direct current measurements presented in the literature [33,36].

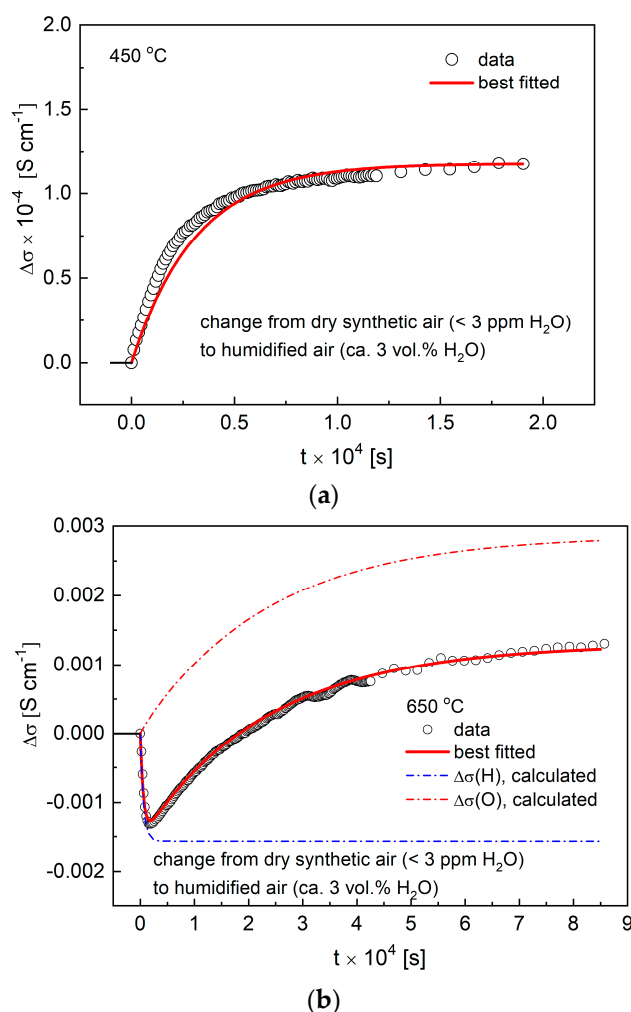


Figure 9. (a) Electrical conductivity relaxation (ECR) data with fit recorded at 450 °C during change of the atmosphere from dry to humidified air; (b) ECR data with fit recorded at 650 °C during change of the atmosphere from dry to humidified air.

All the measured ECR data allowed to prepare the Arrhenius-type graph (Figure 10), in which calculated values of the chemical diffusion coefficient D and the surface exchange coefficient k are presented as a function of temperature. In a range up to 450 °C, in which the single fold relaxation curves were measured, the refined D and k values can be related directly to water, and both coefficients increase with temperature. The activation energy of $D_{\text{H}_2\text{O}}$ in this range was evaluated as 0.77(1) eV. The reported values are comparable in magnitude to the published data for doped BaCeO_3 and similar materials ([30,35] and references therein).

In the 550–700 °C range, the ECR data show decoupled behavior, and transport coefficients can be fitted separately for hydrogen and oxygen, with much higher values (faster diffusion) observed for protons. Such decoupled diffusion was reported previously, e.g., for $\text{SrCe}_{0.95}\text{Yb}_{0.05}\text{O}_{3-a}$ in work [29]. Interested reader can find a detailed theoretical explanation of the nature of decoupling in the cited paper. Interestingly, it seems there is a discontinuity of the D and k values in the intermediate range (a vicinity of 500 °C), which is in accordance with a qualitative change of the nature of the charge carriers diffusion, which takes place when electronic hole-related conductivity becomes significant. Also, as almost no proton-related conductivity component was observed at the highest temperatures (Figure 8a), it is not surprising that ECR at the temperatures above 700 °C do not show an H-related component. Again, the D and k values in this range (corresponding likely to the diffusion of oxygen

only) do not follow linearly values from lower temperatures. In the considered 550–700 °C range, values of the hydrogen- and oxygen-related transport coefficients D and k can be calculated separately for both charge carries (Figure 10). In agreement with literature reports, hydrogen is found to diffuse faster than oxygen during decoupled transport, which manifests itself in a fact that the value of hydrogen-related D is about two orders of magnitude faster than the oxygen-related one. Similar differences, as well as respective orders of magnitude of the transport coefficients were reported before [29,31].

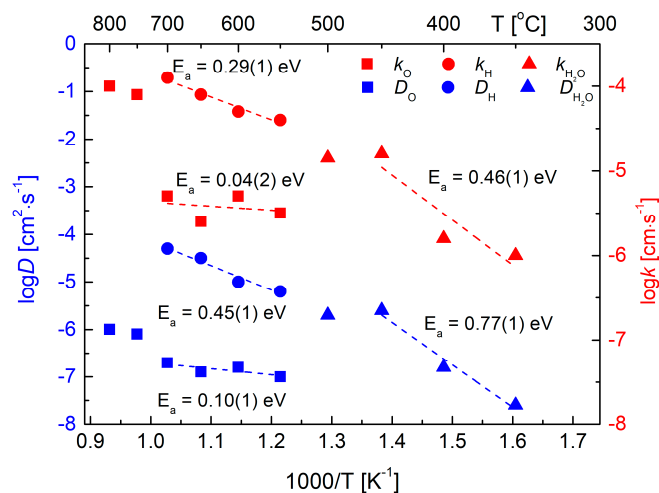


Figure 10. Temperature dependence of the transport coefficients D (blue) and k (red) with calculated values of the activation energy. Please notice description of the used symbols. Data shown in Arrhenius-type coordinates.

As presented above, the nature of the ionic conductivity in $\text{Ba}_{0.9}\text{La}_{0.1}\text{Zr}_{0.25}\text{Sn}_{0.25}\text{In}_{0.5}\text{O}_{3-a}$ is complex and changes with temperature. It depends on the proton content in the material and also on the appearance of the electronic hole-related conductivity at elevated temperatures. As can be expected, diffusion of protons is faster than that of oxygens. However, in the intermediate range at which the decoupling of the ionic charge carriers occurs, the temperature behavior seems non-monotonous.

4. Conclusions

$\text{Ba}_{0.9}\text{La}_{0.1}\text{Zr}_{0.25}\text{Sn}_{0.25}\text{In}_{0.5}\text{O}_{3-a}$ perovskite-type oxide was synthesized and studied in terms of its crystal structure, with RT and high-temperature XRD measurements, its ability for water uptake in different conditions as documented by thermogravimetric measurements with supplementary mass spectroscopy studies, as well as studies of the transport properties in dry, H_2O -, and D_2O -containing air. Single-phase samples were obtained in a wide temperature range of 1200–1600 °C. However, only at the highest temperature was it possible to acquire the dense sinter needed for the electrical measurements. The materials in a powdered form are strongly reacting with moisture from air, which results in a significantly increased unit cell volume. Thermogravimetric studies with analysis of H_2O - and CO_2 -related signals, as well as the high-temperature structural evaluation, confirmed incorporation of water during hydration and presence of protons in the bulk of the material. EIS measurements allowed us to evaluate total electrical conductivity and calculate the values of the activation energy. Also, it was possible to determine proton and deuterium conductivities in wet atmospheres and calculate transference numbers. Importantly, ECR measurements were performed during an abrupt gas change from dry to humidified synthetic air at the constant temperature in a range of 350–800 °C, showing a transition from the single- to two-fold relaxation kinetics. At lower temperatures up to 450 °C, the gathered data allowed us to estimate transport coefficients D and k of water (ambipolar diffusion of H^+ and O^{2-}), while in the 550–700 °C range, it was possible to determine

values of D and k separately for both charge carriers. The coupled/decoupled transition occurring on temperature seems complex, with non-monotonous behavior in the intermediate range observed.

Acknowledgments: This project was funded by the National Science Centre, Poland, on the basis of the decision number DEC-2012/05/E/ST5/03772.

Author Contributions: A.N. and X.L. prepared samples for all measurements. A.N. conducted XRD and TG experiments. W.S. conducted conductivity and relaxation measurements. K.Z. calculated k and D values. K.Ś. analyzed obtained data and wrote the paper.

Conflicts of Interest: The authors declare no conflict of interest.

References

1. Radenahmad, N.; Afif, A.; Petra, P.I.; Rahman, S.M.H.; Eriksson, S.-G.; Azad, A.K. Proton-conducting electrolytes for direct methanol and direct urea fuel cells—A state-of-the-art review. *Renew. Sustain. Energy Rev.* **2016**, *57*, 1347–1358. [[CrossRef](#)]
2. Duan, C.; Tong, J.; Shang, M.; Nikodemski, S.; Sanders, M.; Ricote, S.; Almansoori, A.; O'Hayre, R. Readily processed protonic ceramic fuel cells with high performance at low temperatures. *Science* **2015**, *349*, 1321–1327. [[CrossRef](#)] [[PubMed](#)]
3. Takahashi, T.; Iwahara, H. Proton conduction in perovskite type oxide solid solution. *Rev. Chim. Miner.* **1980**, *17*, 243–253.
4. Iwahara, H.; Uchida, H.; Maeda, N. High temperature fuel and steam electrolysis cells using proton conductive solid electrolytes. *J. Power Sources* **1982**, *7*, 293–301. [[CrossRef](#)]
5. Bonano, N.; Ellis, B.; Mahmood, M.N. Construction and operation of fuel cells based on the solid electrolyte BaCeO₃:Gd. *Solid State Ion.* **1991**, *44*, 305–311. [[CrossRef](#)]
6. Iwahara, H.; Uchida, H.; Yamasaki, I. High-temperature steam electrolysis using SrCeO₃-based proton conductive solid electrolyte. *Int. J. Hydrog. Energy* **1987**, *12*, 73–77. [[CrossRef](#)]
7. Iwahara, H.; Mori, T.; Hibino, T. Electrochemical studies on ionic conduction in Ca-doped BaCeO₃. *Solid State Ion.* **1995**, *79*, 177–182. [[CrossRef](#)]
8. Kreuer, K.D.; Fuchs, A.; Maier, J. HD isotope effect of proton conductivity and proton conduction mechanism in oxides. *Solid State Ion.* **1995**, *77*, 157–162. [[CrossRef](#)]
9. Zajac, W.; Hanc, E.; Gorzkowska-Sobas, A.; Świerczek, K.; Molenda, J. Nd-doped Ba(Ce,Zr)O_{3-δ} proton conductors for application in conversion of CO₂ into liquid fuels. *Solid State Ion.* **2012**, *225*, 297–303. [[CrossRef](#)]
10. Haile, S.M.; West, D.L.; Campbell, J. The role of microstructure and processing on the proton conducting properties of gadolinium-doped barium cerate. *J. Mater. Res.* **1998**, *13*, 1576–1595. [[CrossRef](#)]
11. Iwahara, H.; Yajima, T.; Hibino, T.; Ushida, H. Performance of Solid Oxide Fuel Cell Using Proton and Oxide Ion Mixed Conductors Based on BaCe_{1-x}Sm_xO_{3-α}. *J. Electrochem. Soc.* **1993**, *140*, 1687–1691. [[CrossRef](#)]
12. Liang, K.C.; Nowick, A.S. High-temperature protonic conduction in mixed perovskite ceramics. *Solid State Ion.* **1993**, *61*, 77–81. [[CrossRef](#)]
13. Fabbri, E.; Pergolesi, D.; Traversa, E. Materials challenges toward proton-conducting oxide fuel cells: A critical review. *Chem. Soc. Rev.* **2010**, *39*, 4355–4369. [[CrossRef](#)] [[PubMed](#)]
14. Haile, S.M.; Staneff, G.; Ryu, K.H. Non-stoichiometry, grain boundary transport and chemical stability of proton conducting perovskites. *J. Mater. Sci.* **2001**, *36*, 1149–1160. [[CrossRef](#)]
15. Traversa, E.; Fabbri, E. *Functional Materials for Sustainable Energy Applications*; Kilner, J.A., Skinner, S.J., Irvine, S.J.C., Edwards, P.P., Eds.; Woodhead Publishing Series in Energy, Chapter 16; Woodhead Publishing: Sawston, UK, 2012; pp. 515–537, ISBN 9780857096371.
16. Azad, A.M.; Subramaniam, S.; Dung, T.W. On the development of high density barium metazirconate (BaZrO₃) ceramics. *J. Alloys Compd.* **2002**, *334*, 118–130. [[CrossRef](#)]
17. Norby, T. *Perovskite Oxide for Solid Oxide Fuel Cells*; Ishihara, T., Ed.; Chapter 11; Springer Science Business Media: Berlin, Germany, 2009; pp. 217–241, ISBN 978-0-387-77708-5.
18. Kreuer, K.D. Proton-Conducting Oxides. *Annu. Rev. Mater. Rev.* **2003**, *33*, 333–359. [[CrossRef](#)]
19. Zhu, Z.; Liu, B.; Shen, J.; Lou, Y.; Ji, Y. La₂Ce₂O₇: A promising proton ceramic conductor in hydrogen economy. *J. Alloys Compd.* **2015**, *659*, 232–239. [[CrossRef](#)]

20. Malavasi, L.; Fisher, C.; Saiful Islam, A. Oxide-ion and proton conducting electrolyte materials for clean energy applications: Structural and mechanistic features. *Chem. Soc. Rev.* **2010**, *39*, 4370–4387. [[CrossRef](#)] [[PubMed](#)]
21. Marrony, M. (Ed.) *Proton-Conducting Ceramics: From Fundamentals to Applied Research*; PAN Stanford Publishing: Singapore, 2016; ISBN 9789814613842.
22. Haugsrud, R.; Norby, T. High-temperature proton conductivity in acceptor-doped LaNbO₄. *Solid State Ion.* **2006**, *177*, 1129–1135. [[CrossRef](#)]
23. Quarez, E.; Noirault, S.; Caldes, M.T.; Joubert, O. Water incorporation and proton conductivity in titanium substituted barium indate. *J. Power Sources* **2010**, *195*, 1136–1141. [[CrossRef](#)]
24. Jankovic, J.; Wilkinson, D.P.; Hui, R. Proton conductivity and stability of Ba₂In₂O₅ in hydrogen containing atmospheres. *J. Electrochem. Soc.* **2011**, *158*, B61–B68. [[CrossRef](#)]
25. Geffroy, P.M.; Pons, A.; Bechade, E.; Masson, O.; Fouletier, J. Characterization of electrical conduction and nature of charge carriers in mixed and ionic conductors. *J. Power Sources* **2017**, *360*, 70–79. [[CrossRef](#)]
26. Agmon, N. The Grotthuss mechanism. *Chem. Phys. Lett.* **1995**, *244*, 456–462. [[CrossRef](#)]
27. Kreuer, K.D. *Perovskite Oxide for Solid Oxide Fuel Cells*; Ishihara, T., Ed.; Chapter 12; Springer Science Business Media: Berlin, Germany, 2009; pp. 261–272, ISBN 978-0-387-77708-5.
28. Norby, T.; Widerøe, M.; Glöckner, R.; Larring, Y. Hydrogen in oxides. *Dalton Trans.* **2004**, *19*, 3012–3018. [[CrossRef](#)] [[PubMed](#)]
29. Kim, E.; Yoo, H.I. Two-fold-to-single-fold transition of the conductivity relaxation patterns of proton-conducting oxides upon hydration/dehydration. *Solid State Ion.* **2013**, *252*, 132–139. [[CrossRef](#)]
30. Yoo, H.I.; Yoon, J.Y.; Ha, J.S.; Lee, C.E. Hydration and oxidation kinetics of a proton conductor oxide, SrCe_{0.95}Yb_{0.05}O_{2.975}. *Phys. Chem. Chem. Phys.* **2008**, *10*, 974–982. [[CrossRef](#)] [[PubMed](#)]
31. Yoo, H.I.; Yeon, J.I.; Kim, J.K. Mass relaxation vs. electrical conductivity relaxation of a proton conducting oxide upon hydration and dehydration. *Solid State Ion.* **2009**, *180*, 1443–1447. [[CrossRef](#)]
32. Lee, D.K.; Yoo, H.I. Unusual oxygen re-equilibration kinetics of TiO_{2-δ}. *Solid State Ion.* **2006**, *177*, 1–9. [[CrossRef](#)]
33. Yoo, H.I.; Lee, C.E. Two-Fold Diffusion Kinetics of Oxygen Re-Equilibration in Donor-Doped BaTiO₃. *J. Am. Ceram. Soc.* **2005**, *88*, 617–623. [[CrossRef](#)]
34. Yu, J.H.; Lee, J.S.; Maier, J. Peculiar nonmonotonic water incorporation in oxides detected by local in situ optical absorption spectroscopy. *Angew. Chem. Int. Ed.* **2007**, *46*, 8992–8994. [[CrossRef](#)] [[PubMed](#)]
35. Kreuer, K.D.; Schönherr, E.; Maier, J. Proton and oxygen diffusion in BaCeO₃ based compounds: A combined thermal gravimetric analysis and conductivity study. *Solid State Ion.* **1994**, *70*, 278–284. [[CrossRef](#)]
36. Lim, D.K.; Choi, M.B.; Lee, K.T.; Yoon, H.S.; Wachsmann, E.D.; Song, S.J. Conductivity Relaxation of Proton-Conducting BaCe_{0.85}Y_{0.15}O_{3-δ} Upon Oxidation and Reduction. *J. Electrochem. Soc.* **2011**, *158*, B852–B856. [[CrossRef](#)]
37. Singh, K.K.; Ganguly, P.; Rao, C.N. Structural transitions in (La,Ln)₂CuO₄ and La₂(Cu,Ni)O₄ systems. *Mater. Res. Bull.* **1982**, *17*, 493–500. [[CrossRef](#)]
38. Kanai, H.; Mizusaki, J.; Tagawa, H.; Hoshiyama, S.; Hirano, K.; Fujita, K.; Tezuka, M.; Hashimoto, T. Defect Chemistry of La_{2-x}Sr_xCuO_{4-δ}: Oxygen Nonstoichiometry and Thermodynamic Stability. *J. Solid State Chem.* **1997**, *131*, 150–159. [[CrossRef](#)]
39. Colombari, P.; Tran, C.; Zaafrani, O.; Slodczyk, A. Aqua oxyhydroxycarbonate second phases at the surface of Ba/Sr-based proton conducting perovskites: A source of confusion in the understanding of proton conduction. *J. Raman Spectrosc.* **2013**, *44*, 312–321. [[CrossRef](#)]
40. Zhang, G.B.; Smyth, D.M. Protonic conduction in Ba₂In₂O₅. *Solid State Ion.* **1995**, *82*, 153–160. [[CrossRef](#)]
41. Crank, J. *The Mathematics of Diffusion*, 2nd ed.; Oxford University Press: New York, NY, USA, 1975; ISBN 0198533446.
42. Han, D.; Majima, M.; Uda, T. Structure Analysis of BaCe_{0.8}Y_{0.2}O_{3-δ} in Dry and Wet Atmospheres by High-Temperature X-ray Diffraction Measurement. *J. Solid State Chem.* **2013**, *205*, 122–128. [[CrossRef](#)]
43. Świerczek, K.; Skubida, W.; Niemczyk, A.; Olszewska, A.; Zheng, K. Structure and transport properties of proton-conducting BaSn_{0.5}In_{0.5}O_{2.75} and A-site substituted Ba_{0.9}Ln_{0.1}Sn_{0.5}In_{0.5}O_{2.8} (Ln = La, Gd) oxides. *Solid State Ion.* **2017**, *307*, 44–50. [[CrossRef](#)]
44. Skubida, W.; Świerczek, K. Structural properties and presence of protons in Ba_{0.9}Gd_{0.1}Zr_{1-x-y}Sn_xIn_yO_{3-(y-0.1)/2} perovskites. *Funct. Mater. Lett.* **2016**, *9*, 1641005. [[CrossRef](#)]

45. Andersson, A.K.E.; Selbach, S.M.; Knee, S.C.; Grande, T. Chemical Expansion Due to Hydration of Proton-Conducting Perovskite Oxide Ceramics. *J. Am. Ceram. Soc.* **2014**, *97*, 2654–2661. [[CrossRef](#)]
46. Han, D.; Shinoda, K.; Uda, T. Dopant Site Occupancy and Chemical Expansion in Rare Earth-Doped Barium Zirconate. *J. Am. Ceram. Soc.* **2014**, *97*, 643–650. [[CrossRef](#)]
47. Kreuer, K.D. On the complexity of proton conduction phenomena. *Solid State Ion.* **2000**, *136*, 149–160. [[CrossRef](#)]
48. Babilo, P.; Uda, T.; Haile, S.M. Processing of yttrium-doped barium zirconate for high proton conductivity. *J. Appl. Phys.* **2007**, *22*, 1322–1330. [[CrossRef](#)]



© 2018 by the authors. Licensee MDPI, Basel, Switzerland. This article is an open access article distributed under the terms and conditions of the Creative Commons Attribution (CC BY) license (<http://creativecommons.org/licenses/by/4.0/>).